inorganics

MDPI

Article

Dielectric Spectroscopy of Non-Stoichiometric $SrMnO_3$ Thin Films

Shuang Zeng [1], Jing Yang [1,2,*], Qingqing Liu [1], Jiawei Bai [1], Wei Bai [1], Yuanyuan Zhang [1] and Xiaodong Tang [1,3,*]

[1] Key Laboratory of Polar Materials and Devices (MOE), Department of Electronic Science, East China Normal University, Shanghai 200241, China
[2] Chongqing Key Laboratory of Precision Optics, Chongqing Institute of East China Normal University, Chongqing 401120, China
[3] Collaborative Innovation Center of Extreme Optics, Shanxi University, Taiyuan 030006, China
* Correspondence: jyang@ee.ecnu.edu.cn (J.Y.); xdtang@sist.ecnu.edu.cn (X.T.)

Abstract: The dielectric properties of non-stoichiometric $SrMnO_3$ (SMO) thin films grown by molecular beam epitaxy were systematically investigated. Especially, the effects of cation stoichiometry-induced diverse types and densities of defects on the dielectric properties of SMO films were revealed. Two anomalous dielectric relaxation behaviors were observed at different temperatures in both Sr-rich and Mn-rich samples. High-temperature dielectric relaxation, resulting from a short-range Mn-related Jahn–Teller (JT) polaron hopping motion, was reinforced by an enhancement of JT polaron density in the Sr-rich film, which contained abundant SrO Ruddlesden–Popper (R-P) stacking faults. However, an excessive number of disordered Sr vacancy clusters in Mn-rich thin film suppressed the hopping path of JT polarons and enormously weakened this dielectric relaxation. Thus, The Sr-rich film demonstrated a higher dielectric constant and dielectric loss than the Mn-rich film. In addition, low-temperature dielectric relaxation may be attributed to the polarization/charge glass state.

Keywords: dielectric property; non-stoichiometry; perovskite manganese oxide

Citation: Zeng, S.; Yang, J.; Liu, Q.; Bai, J.; Bai, W.; Zhang, Y.; Tang, X. Dielectric Spectroscopy of Non-Stoichiometric $SrMnO_3$ Thin Films. *Inorganics* **2024**, *12*, 71. https://doi.org/10.3390/inorganics12030071

Academic Editor: Kazuyuki Takahashi

Received: 20 January 2024
Revised: 21 February 2024
Accepted: 24 February 2024
Published: 27 February 2024

1. Introduction

The strong electronic correlation properties of transition metal oxides are considered a focal point in condensed matter physics and solid-state electronic device applications. There exists a delicate equilibrium of competition among diverse phase structures and strong coupling between spin, charge, orbit, and lattice in these electronic correlation systems [1]. Such balance is easily disrupted by minute external factors, such as stress, electric fields, temperature fields, and chemical doping, resulting in significant alterations in physical properties [2]. These changes give rise to distinctive quantum effects including the metal–insulator transition, giant magneto-resistance, charge-ordering disorder, and multiferroicity, etc. [3–5]. The aforementioned novel features are anticipated to be applied in the next generation of multifunctional microelectronics, energy applications, optoelectronics, and quantum security applications [6–9].

In addition to the inherent physical mechanism of strong electronic correlation, related defects, which are observed in perovskite oxides, including Ruddlesden–Popper (R-P) stacking faults, A-vacancy clusters, oxygen vacancies, and stress-induced array defects, also play a primary role in achieving or enhancing the unique physical properties of perovskite oxides. Particularly, defects can significantly enhance the perturbation effects of the external multi-fields (such as electric field, magnetic field, and strain) in the oxides, providing a route to control new functionalities [10]. Generally, the chemical compositions, modified slightly, can provoke the formation of defects, which subsequently lead to alterations in physical properties. For example, carrier concentration and bandgap can be directly impacted by inducing lattice distortions through defects in non-stoichiometric conditions [11]. Anionic

vacancies can induce a transition from the non-magnetic state to the magnetic state [12–14], or the metal–insulator phase transition [15]. Malyi et al. [11] have highlighted that cationic vacancies can create new sublattices and ordered vacancy compounds spontaneously when a significant deviation from the normal stoichiometric ratio is present in the $A_{1-\delta}B_{1-\gamma}O_3$ system (δ and/or $\gamma > 1\%$). For the stable degenerate Ba-Nb-O gapped compounds, the increase in Ba or Nb vacancy concentration and formation of order vacancy compounds noticeably alter the optoelectronic properties via modifying the material band structure. The compounds containing these cationic vacancies exhibit the lowest average absorption coefficients in the visible range [16]. The in-plane phase separation in Li_xCoO_2 ($0.5 < x < 1$) results in a kinetically arrested state, while defects such as interstitials and Co^{4+} vacancies can induce reorientation of the phase boundary to achieve the theoretical minimum-energy configuration, leading to a metal–Mott insulator transition to achieve multiple conductivity states, which could be efficient memristors [17]. Li et al. [18] manipulated the local Sr/Ti molar ratio of $SrTiO_3$-based films via pulsed-laser deposition to induce Ti/O defects, so that coexisting spin and dipole reentrant glass states were realized. Moreover, the occurrence of oxygen vacancies, the most common defects in perovskite oxides, is also inevitable in the process of material preparation. The macroscopic properties can be affected by oxygen vacancies, such as catalytic [19], electrical [20,21], magnetic [22,23], and transport [24,25] properties of the film.

Strained $SrMnO_3$ (SMO) film as a typical perovskite manganese oxide, has been verified to be multiferroic through the first-principles calculations (coexistence of magnetic and ferroelectric orders) [26] and experimental investigation [13,27]. In addition to the strain factor, the non-stoichiometric ratio of cations and oxygen deficiency induce the generation of various defect states, and defect-driven multivalent ion states play a crucial role in polarization and spin ordering [28]. The responses of electrical/spin polarizations in multiferroics to various external fields are central topics in basic physics and potential technological applications. Especially, dielectric responses/properties in the multiferroic materials reveal the dynamic responses of electrical polarization to a small AC electric field. Dielectric spectroscopy measurement of dielectric response is indispensable in investigating multiferroic materials and serves as a powerful tool for elucidating the underlying physical mechanisms governing diverse enigmatic phenomena and properties, such as ferric domain wall motion, heterogeneous interface effects, the transport mechanisms of localized charged carriers and polarons, and so on. Considering the distinct electrical behaviors exhibited in non-stoichiometric films, various peculiar phenomena often coincide with anomalous behavior in dielectric responses. Therefore, investigating variations in the dielectric constant and loss can offer profound insights into the characteristics of defects induced by different stoichiometries and their effects on electrical characteristics in perovskite oxides. However, the charge transport and dielectric mechanisms in non-stoichiometric SMO systems have not yet been established. In this work, we present the temperature-dependent and frequency-dependent dielectrics of SMO (001) non-stoichiometric ultra-thin films. A detailed quantitative analysis was conducted on the multiple dielectric relaxations (DRs) and local charged carrier/defect migration behavior below room temperature to reveal the correlation between cation stoichiometry-induced defects and dielectric behavior. It is imperative to systematically analyze dielectric anomalies in non-stoichiometric films. This analysis not only provides some insights to elucidate strongly correlated complex interactions and relevancies between defects, localized charge carriers, and multivalent Mn ions, but also serves as a versatile platform for observing localized charge carrier motion and charge transfer, which can provide experimental support for the determination of carrier transport behavior and guide for the functional applications of non-stoichiometric oxides in electrocatalysis, energy storage, resistive switching, and memory devices, etc.

2. Results and Discussion

2.1. Structure Characterization

Figure 1 shows the θ-2θ X-ray diffraction scans of SMO thin films under different Sr/Mn ratios. Overall, the X-ray diffraction (XRD) patterns of all three samples reveal distinct Kiessig oscillations on the edges of the peaks, indicating the excellent crystal quality of the samples and high quality at the SMO/Nb: $SrTiO_3$ (NSTO) interface. The (002) peak of SMO film with a stoichiometric ratio (Sr/Mn = 1:1) can be observed at 48.34° in Figure 1b, indicating an out-of-plane lattice constant of 3.763 Å, and suggests a higher tensile strain in the in-plane direction. The (002) XRD peak sites of SMO film shift towards lower angles in non-stoichiometric samples compared to those of stoichiometric ones. The out-of-plane lattice constant is 3.773 Å in Sr-rich film (Figure 1a), which indicates a significant strain relaxation accompanied by increased interplanar spacing and the occurrence of lattice expansion [10,29,30]. The Mn-rich sample exhibits a relatively maximum lattice constant, which is calculated to be 3.778 Å, as shown in Figure 1c. In general, the variation in the lattice constants in oxide thin films is generally attributed to the oxygen vacancies (OVs) and cation stoichiometry [31,32]. In the present case, it is inevitable that many OVs within the SMO film will be created in the growth process of oxide films. Consequently, it gives rise to a certain extent of lattice expansion and induces chemical valence alterations in Mn ions [12,33,34]. Moreover, different cation stoichiometry may also result in a certain amount of defects, such as rock salt planes (R-P planar faults) or cation vacancy defect clusters, to whom the deviations in lattice constants among SMO thin films can be also attributed.

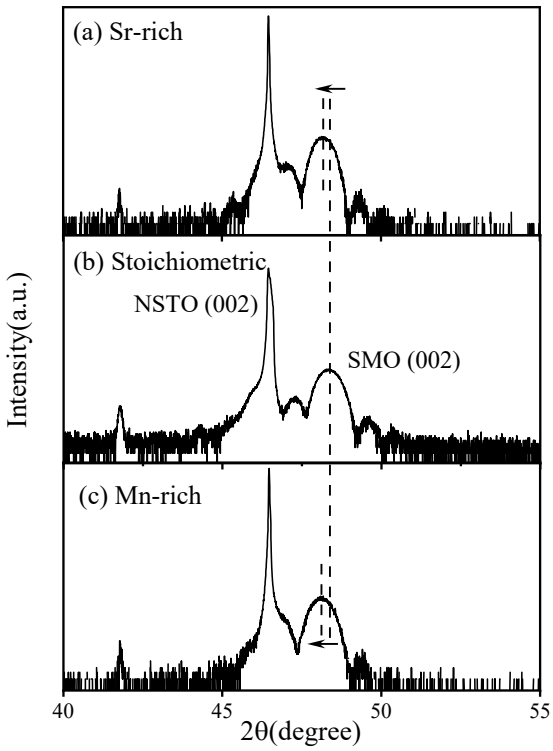

Figure 1. X-ray diffraction θ-2θ scans for (**a**) Sr-rich, (**b**) stoichiometric, and (**c**) Mn-rich SMO thin films with out-of-plane (002) reflection. The dotted line indicates the position of the peak, while the arrow denotes its movement.

The lattice expansion implied by the XRD peak shifts of non-stoichiometric SMO films was then investigated through a comprehensive microstructural analysis using high-resolution transmission electron microscopy (TEM). It can be observed that numerous line dislocations in horizontal or vertical directions occurred in the Sr-rich SMO film (Figure 2a). These horizontal or vertical dislocations may originate from excess Sr-site ions. Since the

formation energy of Mn-site vacancies is higher, excess Sr-site ions prefer to be incorporated by binding with O ions, forming SrO rock salt planes, namely Ruddlesden–Popper (R-P) stacking faults, which is consistent with related reports on A-site-rich perovskite oxides [32,35]. During the initial stages of thin film growth, SrO R-P stacking faults tend to grow in the vertical direction, because the large lattice size of SrO R-P stacking faults can compensate for the in-plane lattice mismatch between SMO films and STO substrates and, therefore, relax tensile strain. Following that, the horizontal SrO R-P stacking faults begin to form. Undoubtedly, either horizontal or vertical SrO R-P stacking faults can result in lattice expansion in Sr-rich SMO films. In addition, it can be inferred that the appearance of SrO R-P stacking faults consumes O ions too much for binding with rich Sr ions, which brings about more oxygen deficiency in perovskite SMO lattices and produces a higher density of OVs. The generation of excess OVs further aggravates lattice expansion. Figure 2b shows the clear TEM image contrast in the Mn-rich film. Generally, perovskite oxides with excess B-site elements existing during growth tend to exhibit a propensity for the formation of A-site vacancies [36]. This may be interpreted as the formation of Sr vacancies (V_{Sr}s) and accompanying large-scale disordered structural defects. The accumulation of Sr vacancies expands the lattice locally with the help of Coulomb repulsion and results in large-scale disordered structural defects [32,37]. Similar phenomena have also been reported in Ti-rich $SrTiO_3$ films. Tsuyoshi et al. propose that the preferential formation of Sr vacancies is the most plausible scenario in cases of excess B-site Ti, as the generation of interstitial Ti contradicts the principle of energy minimization and the formation of Sr vacancies conductive to the stabilization of such B-site-rich perovskite oxides systems [32]. Tokuda et al. found that an excess of B-site elements leads to a decrease in the intensity and an increase in the width of the characteristic peaks of the O-K electronic energy loss near-edge structure in $SrTiO_3$, confirming that V_{Sr} are introduced into $SrTiO_3$ thin film containing an excess of Ti and form clusters [36]. Therefore, Sr vacancy clusters and large-scale disordered structural defects may lead to lattice expansion in Mn-rich SMO films, which is consistent with earlier reports [38].

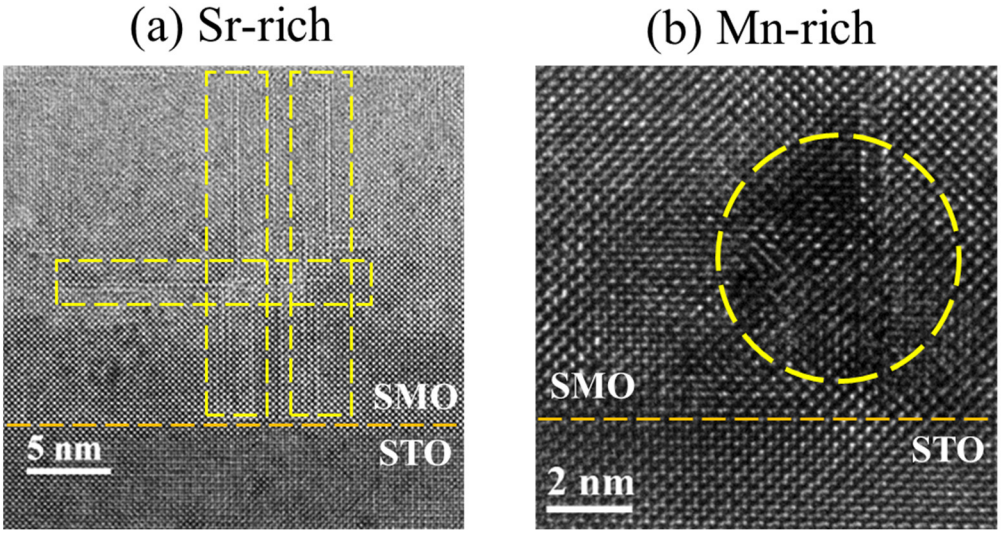

Figure 2. Cross-sectional high-resolution TEM images of (**a**) Sr-rich, (**b**) Mn-rich SMO films. The orange dashed lines highlight the interface, while the yellow dashed lines emphasize the defects.

2.2. Dielectric Characterization

It is well known that the presence and migration of these defects have a prominent impact on the electrical properties of the films. Investigating the electrical properties of the non-stoichiometric SMO films mentioned above not only can further validate the defect types, but also reveal how cation ratios impact electrical characteristics. Thus, analyses of the frequency and temperature dependence of the dielectric properties of the

Sr-rich and Mn-rich films were performed. The temperature dependences of the real dielectric constant (ε') in non-stoichiometric SMO films at various frequencies are shown in Figure 3a,c. Overall, the dielectric constant exhibited a pronounced decrease with the decreases in the temperature and significant dispersion (ε' underwent a decrease with increasing frequency). The Sr-rich film exhibits two distinct plateau regions at low and high temperatures in Figure 3a, corresponding to two sets of abnormal dielectric loss (tanδ) peaks in the same temperature (Figure 3b) region. The temperature of the loss peak shifted to higher temperatures with increasing frequency, demonstrating typical thermal activation characteristics. The above-mentioned dielectric phenomena are representative features of dielectric relaxation [39]. Here, the dielectric relaxation at a low temperature is designated as DR1, while dielectric relaxation at a high temperature is designated as DR2. As for the Mn-rich SMO sample, the ε' and tanδ vs. temperature curves also present a prominent DR1, but a very weak DR2 (Figure 3d), and both relaxation dynamics are similar to the counterparts of the Sr-rich sample. Comparing non-stoichiometric SMO films, the values of the ε' and tanδ of the Mn-rich sample were significantly reduced by half compared with the Sr-rich SMO film. And the relaxation strength of DR2 in the Mn-rich sample was extremely suppressed; however, the relaxation strength of DR1 remained unchanged.

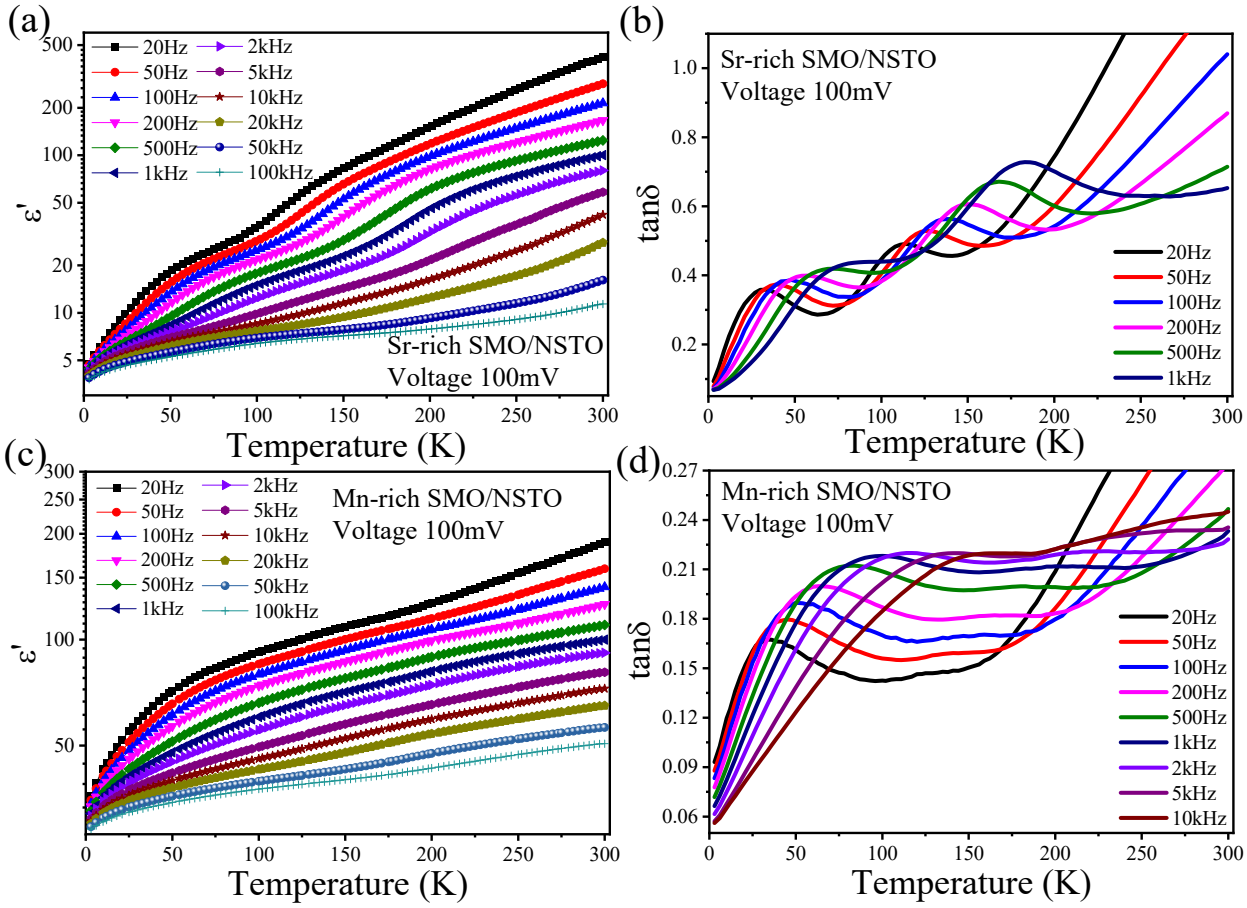

Figure 3. Temperature dependence of (**a**) ε' and (**b**) tanδ in Sr-rich SMO/NSTO film at various frequencies. Temperature dependence of (**c**) ε' and (**d**) tanδ in Mn-rich SMO/NSTO film at various frequencies.

Figure 4a shows the frequency-dependent dielectric constant (ε') and loss (tanδ) of the Sr-rich SMO film at various temperatures from 50 to 300 K. As the temperature approaches room temperature, the variation in the dielectric constant with the frequency becomes more pronounced, and the dielectric dispersion becomes increasingly apparent. A similar trend is also evident in the dielectric spectroscopy of the Mn-rich sample, as shown in Figure 4b.

The frequency-dependent dielectric loss also shows two distinct dielectric loss peaks. Furthermore, the relaxation frequencies corresponding to the loss peaks increase when the temperature rises, fully demonstrating that the low-frequency dielectric dispersion and dielectric loss peak in non-stoichiometric SMO thin films originate from dielectric relaxation, as shown in Figure 3. To further obtain the relaxation parameters, the frequency-dependent dielectric spectroscopy was fitted utilizing the Cole–Cole function [40,41],

$$\varepsilon^* = \varepsilon_\infty + \Delta\varepsilon/[1 + (j\omega\tau)^{1-\alpha}], \quad (1)$$

where $\Delta\varepsilon = \varepsilon_s - \varepsilon_\infty$ is the dielectric relaxation strength ε_s and ε_∞ are static and high-frequency dielectric constants. j is the square root of -1, ω is the angular frequency, and α is the degree of distribution of relaxation time (τ). Colorful solid lines represent good fitting results of the Cole–Cole function. Dielectric relaxation strength $\Delta\varepsilon$ values obtained based on the frequency spectrum, shown in Figure 4, are 414.8 for the Sr-rich sample and 150.9 for the Mn-rich film at room temperature, respectively, which shows that the dielectric constant, loss, and DR2 relaxation strength of Mn-rich film are indeed restrained and are much smaller than those of Sr-rich film. Based on the above-mentioned experimental evidence, some reliable conclusions can be drawn, as follows. Cation stoichiometry plays a significant role in the dielectric properties of SMO films. DR2 may be rooted in the motions of defect-related relaxation entities, whereas DR1 may result from an intrinsic physical process free from the effects of related defects in SMO films.

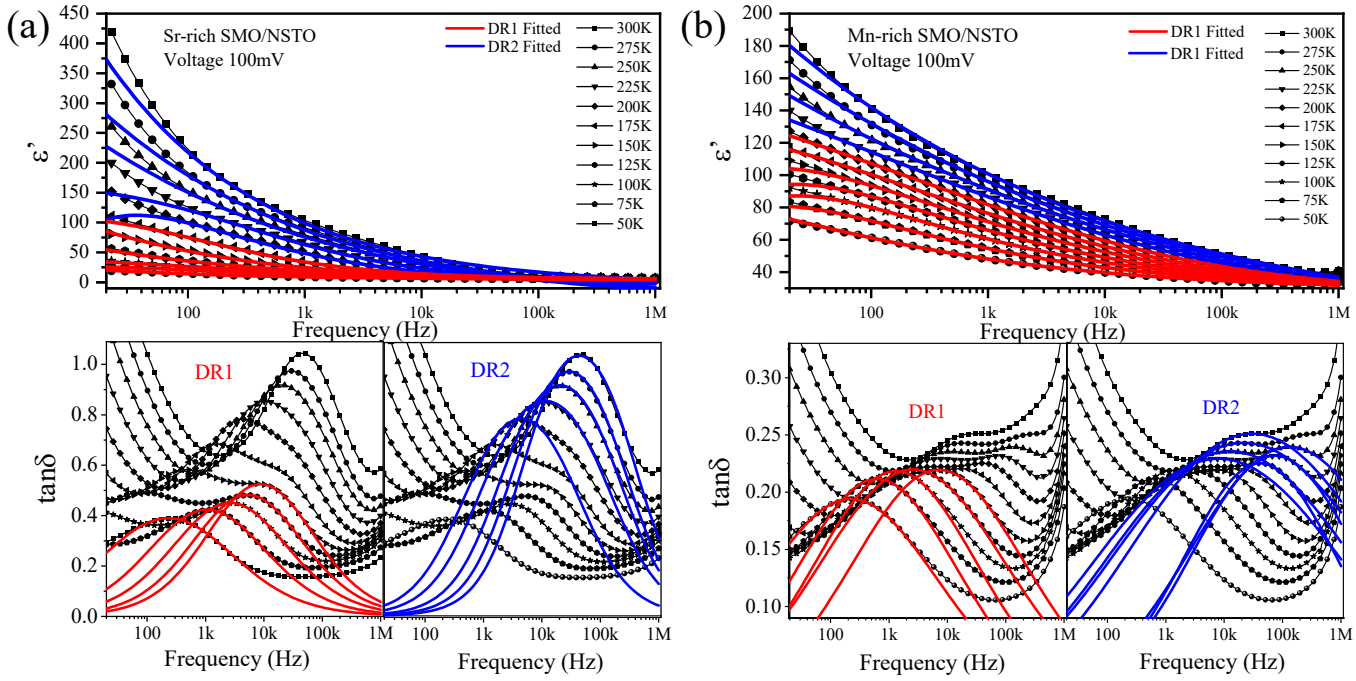

Figure 4. Frequency dependence of ε' and tanδ in (**a**) Sr-rich SMO/NSTO film and (**b**) Mn-rich SMO/NSTO film at various temperatures. Colored lines are the fitting curves of the Cole–Cole function.

2.3. Relaxation Mechanism Analysis

Generally, dielectric relaxation mechanisms can be broadly classified into two categories. The first type originates from Maxwell–Wagner (MW) interfacial relaxation at heterogeneous interfaces [42], such as the interfaces between grains and grain boundaries. The other type is associated with localized polarization entities within the films, such as localized carrier migration, charged defects and defect complex motion, the movement of ferroelectric domain walls, nano-scale polarization/polarized glass state, etc. [43–48].

Generally, MW relaxation can be discriminated by successively observing several distinct arcs of heterogeneous components in Nyquist diagrams of complex-plane impedance with the change in measured frequency [49,50]. The complex impedance spectroscopy of the samples at DR-occurring temperatures and frequencies was examined to probe the MW effect, as shown as Figure 5. The Sr-rich sample shows only a 1/4 arc at high temperatures, and exhibits a large oblique line with one incomplete semi-circular arc at low temperatures, while the Mn-rich film exhibited one incomplete semicircle at both high and low temperatures. This suggests that the dielectric response in the current temperature and frequency predominantly arises from film bulk effects, rather than being influenced by heterogeneous structures. Consequently, the contribution of the Maxwell–Wagner mechanism to dielectric relaxation can be ruled out.

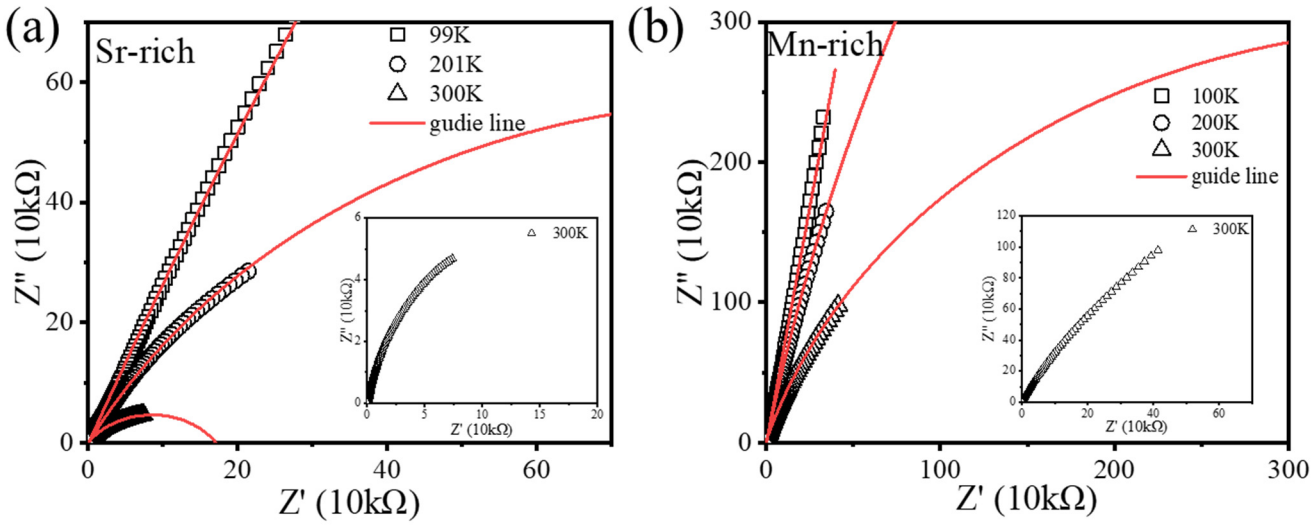

Figure 5. Nyquist diagrams of the complex-plane impedance of the (**a**) Sr-rich thin film and (**b**) Mn-rich thin film.

In addition, the dielectric relaxation induced by the movement of ferroelectric domain walls often occurs at high frequencies (above MHz), and also should be removed from the list of possible causes of the present relaxation mechanism. And given the above-mentioned experimental evidence, localized carrier migration, charged defects/defect complex motion and nanoscale polarization/polarized glass state may be the possible origins for DR1 and DR2. To confirm the mechanisms of DR1 and DR2, the relaxation thermodynamics of the two relaxations were fitted using the Arrhenius relation and the glass-type critical power law, respectively.

The Arrhenius relation is utilized to examine relaxation thermodynamics of the films, with the following formula:

$$f_r = f_0 \exp(-\frac{E_a}{k_B T}) \quad (2)$$

where f_r is the relaxation frequency, E_a is the activation energy, f_0 is the factor, and k_B is the Boltzmann constant [48,49]. The ln (f_r)−1000/T curves corresponding to non-stoichiometric SMO films were extracted in the frequency–dielectric spectrum, and a linear fitting was performed. The activation energy of the Sr-rich SMO film was ~0.12 eV, while that of the Mn-rich SMO film was ~0.14 eV (Figure 6), which closely resembles the relaxation activation energy associated with the Jahn–Teller (JT) polaron hopping related to Mn^{3+} ions in manganese oxide systems, as has been reported [51–53]. The JT polaron in manganese compounds is commonly associated with the Jahn–Teller distortion often observed in the Mn^{3+}-O octahedron. Due to Jahn–Teller distortion, the decrease in crystal symmetry leads to the degeneration of electron orbitals and a reduction in the energy of electron-occupied states. The electron–phonon coupling at this stage is induced by the Coulomb effect of

lattice vibrations on the e_g orbital electrons, which are captured by Jahn–Teller distortion. The captured electrons and Jahn–Teller distortion collectively consist of the JT polaron, which exhibits a short-range hopping behavior akin to the reorientation motion of electrical dipoles in an applied AC electric field. When the frequency of the increased AC electric field approaches or exceeds the hopping frequency of the JT polaron, the hopping motion of the JT polaron fails to follow the field, resulting in a dielectric relaxation [54]. During this process, the contribution of JT polaron short-range hopping to dielectric properties becomes weak, resulting in a gradual reduction in the dielectric constant. Because of the fact that the interaction between the reorientation dipoles (namely, JT polaron short-range hopping here) and the surrounding medium is dynamically frictional in nature, dielectric relaxation is accompanied by an energy dissipation process and can be observed in the peaks in the dielectric loss. As usual, SMO contains only Mn^{4+} ions. However, positively charged oxygen vacancies, which cannot be unavoidable in oxide SMO, can induce the transition from Mn^{4+} to Mn^{3+} ions to maintain the electrical neutrality of the system. X-ray photoelectron spectroscopy investigation [33] and the weak ferromagnetic phase induced by the Mn^{3+}-O-Mn^{4+} double exchange of the SMO thin films [12] provide the evidence for the rationality behind the existence of Mn^{3+}-related JT polarons. The origin of DR2 can be attributed to the short-range hopping motion of the JT polaron. According to the aforementioned defect analysis, excess Sr ions in Sr-rich film prefer to be incorporated by binding with O ions because of the low formation energy of Sr-O; therefore, horizontal or vertical SrO R-P stacking faults appear. The formation of SrO R-P stacking faults undoubtedly consumes O ions excessively, resulting in the generation of additional oxygen vacancies in SMO lattices. More oxygen vacancies would bring about more Mn^{3+}-related JT polarons. Therefore, Jahn–Teller polaron hopping-induced dielectric relaxation in Sr-rich SMO films is more pronounced at a low frequency, which leads to increases in the dielectric constant and loss. In the Mn-rich SMO film, the hopping path of JT polarons was limited by large-scale disordered structural defects and Sr vacancy clusters, resulting in a certain inhibition of dielectric relaxation at the low frequency [32]. Consequently, there was a decrease observed in both the dielectric constant and dielectric loss of the film. This is the reason why the Mn-rich film had a relatively small dielectric constant and loss compared to the Sr-rich SMO, as can be observed in Figure 4.

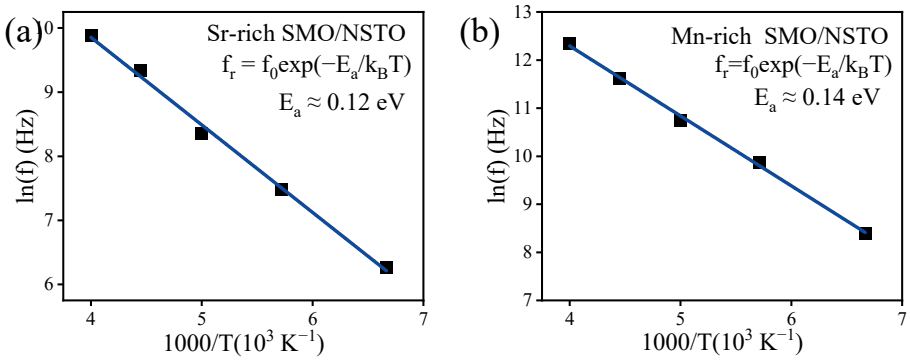

Figure 6. (**a**) and (**b**) show the Arrhenius plots of DR2 for the Sr-rich and Mn-rich samples.

Relaxation thermodynamics of DR1 can be described by the function of the glass-type critical power law as

$$f_r = a(T - T_0)^n \quad (3)$$

where a is a factor, T_0 is the zero-frequency freezing temperature, and n depends on the particular system and is related to the standard spatial correlation length critical exponent [47,55]. The parameters T_0 of the Sr-rich and Mn-rich films calculated by fitting are ~29 K and 25 K (Figure 7) in DR1, which is consistent with the result of the stoichiometry sample (~28 K) [33]. The fitting parameters n are 2.16 (Sr-rich) and 2.55 (Mn-rich), in accordance with previous findings [47]. The displacement of Mn ions from the center of the

Mn-O octahedron induces electrical polarization in SMO films under stress, while a robust spin-lattice interaction is exhibited. The spin glass state at low temperatures decelerates the fluctuations of local polarization, leading to the possibility of multiple glass states in SMO films. Consequently, it can be inferred that DR1 originates from the relaxation of the polarized glass state.

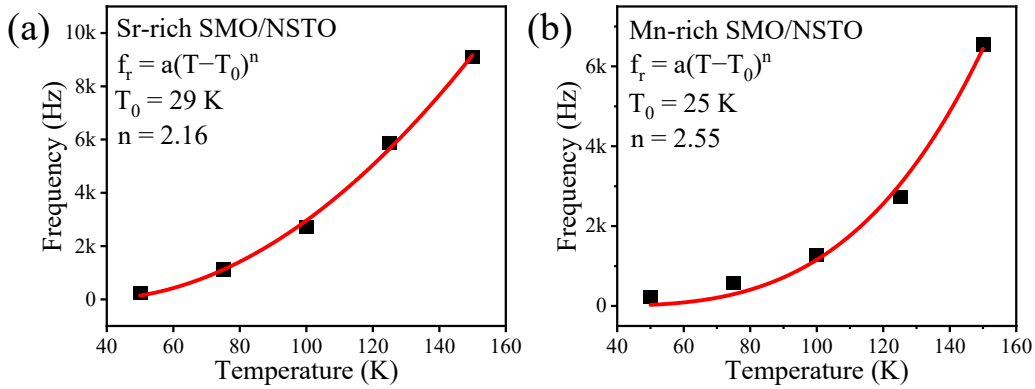

Figure 7. The *fr–T* curves of DR1 in (**a**) Sr-rich SMO/NSTO film and (**b**) Mn-rich SMO/NSTO film are fit using the critical power law, respectively.

3. Experimental Procedure

$SrMnO_3$ (SMO) films were grown at 750 °C by a molecular beam epitaxy (MBE) system (Riber, Bezons, France) on the Nb: $SrTiO_3$ (NSTO) (001) substrates. In an oxygen atmosphere, the Sr source and Mn source opened in turn to form SMO (001) thin films. The pressure of Sr and Mn evaporation sources remained constant throughout the growth process at values of 5×10^{-8} and 3×10^{-8} Torr, respectively. We use atomic alternating-layer shuttered MBE to achieve precise cation stoichiometry [26]. The cation stoichiometric ratio was adjusted by controlling the opening/closing time of the shutters and the real-time growth was observed in situ by reflection high-energy electron diffraction (RHEED) oscillations, which depend on the chemical mean inner potential energy divergence between different cation sub-monolayers/terminations. The Mn cation ratios [Mn/(Sr + Mn)] of the Sr-rich and Mn-rich samples were 48.22% and 51.67%, respectively. The structure quality of the SMO thin films was characterized using XRD (Bruker, Beijing, China) with Cu Kα radiation. High-resolution TEM was carried out using a JEOL (Tokyo, Japan) electron microscope operated at 200 kV. Utilizing masks and ion sputtering, Pt electrodes were deposited on the surface of SMO thin films, forming a planar capacitance device structure for dielectric testing. Dielectric properties were measured using an impedance analyzer (Agilent, Penang, Malaysia) combined with a physical property measurement system (PPMS-9, Quantum Design), San Diego, CA, America) from 3 K to 300 K.

4. Conclusions

Atomic alternating-layer shuttered molecular beam epitaxy was employed to achieve precise stoichiometry. There were SrO R-P stacking faults in the Sr-rich thin film, and disordered Sr vacancy clusters occurred in the Mn-rich SMO. The dielectric properties of SMO films are significantly influenced by varying cation stoichiometric ratios. Although both Sr-rich and Mn-rich films exhibited two types of anomalous dielectric relaxation peaks in temperature- and frequency-dependent dielectric responses, the Sr-rich film demonstrated a higher dielectric constant and dielectric loss than those of the Mn-rich film. Although the dielectric relaxation at high temperature, which derived from short-range Mn-related Jahn–Teller (JT) polaron hopping, was more pronounced in Sr-rich film, the counterpart in Mn-rich film was significantly suppressed. These stoichiometry-dependent results are closely associated with the diverse types and densities of defects. SrO R-P stacking faults in the Sr-rich film resulted in an increased number of oxygen vacancies and, thereby, the density of Mn^{3+} ions, reinforcing the short-range Mn-related JT polaron

hopping and high-temperature dielectric relaxation. Thus, The Sr-rich film demonstrated a higher dielectric constant and dielectric loss. However, an excessive number of disordered Sr vacancy clusters in Mn-rich thin film suppressed the hopping path of JT polarons and enormously weakened the dielectric relaxation, giving rise to the decreases in the dielectric constant and loss. In addition, low-temperature dielectric relaxation may be attributed to the polarization/charge glass state.

Author Contributions: Investigation, S.Z., Q.L. and J.B.; Writing—original draft, S.Z.; Writing—review & editing, J.Y.; Supervision, W.B. and Y.Z.; Project administration, X.T. All authors have read and agreed to the published version of the manuscript.

Funding: The work is supported by the Natural Science Foundation of Chongqing (CSTB2022NSCQ-MSX0589 and CSTB2022NSCQ-MSX1474), the National Science Foundation of China (61574058 and 61674058), and the ECNU (East China Normal University) Multifunctional Platform for Innovation (006).

Data Availability Statement: Data are contained within the article.

Acknowledgments: We would like to thank the Natural Science Foundation of Chongqing, the National Science Foundation of China, and the ECNU (East China Normal University) Multifunctional Platform for Innovation (006).

Conflicts of Interest: The authors declare no conflict of interest.

References

1. Lee, J.H.; Ke, X.; Misra, R.; Ihlefeld, J.F.; Xu, X.S.; Mei, Z.G.; Heeg, T.; Roeckerath, M.; Schubert, J.; Liu, Z.K.; et al. Adsorption-controlled growth of $BiMnO_3$ films by molecular-beam epitaxy. *Appl. Phys. Lett.* **2010**, *96*, 262905. [CrossRef]
2. Pashchenko, A.V.; Liedienov, N.A.; Li, Q.; Makoed, I.I.; Tatarchuk, D.D.; Didenko, Y.V.; Gudimenko, A.I.; Kladko, V.P.; Jiang, L.; Li, L.; et al. Control of dielectric properties in bismuth ferrite multiferroic by compacting pressure. *Mater. Chem. Phys.* **2021**, *258*, 123925. [CrossRef]
3. Burschka, J.; Pellet, N.; Moon, S.J.; Humphry-Baker, R.; Gao, P.; Nazeeruddin, M.K.; Gratzel, M. Sequential deposition as a route to high-performance perovskite-sensitized solar cells. *Nature* **2013**, *499*, 316–319. [CrossRef]
4. Lee, M.M.; Teuscher, J.; Miyasaka, T.; Murakami, T.N.; Snaith, H.J. Efficient Hybrid Solar Cells Based on Meso-Superstructured Organometal Halide Perovskites. *Science* **2012**, *338*, 643–647. [CrossRef]
5. Goldschmidt, V.V.M. Die Gesetze der Krystallochemie. *Naturwissenschaften* **1926**, *14*, 477–485. [CrossRef]
6. Zhao, X.N.; Xu, H.Y.; Wang, Z.Q.; Lin, Y.; Liu, Y.C. Memristors with organic-inorganic halide perovskites. *InfoMat* **2019**, *1*, 183–210. [CrossRef]
7. Deng, W.; Jin, X.C.; Lv, Y.; Zhang, X.J.; Zhang, X.H.; Jie, J.S. 2D Ruddlesden–Popper Perovskite Nanoplate Based Deep-Blue Light-Emitting Diodes for Light Communication. *Adv. Funct. Mater.* **2019**, *29*, 1903861. [CrossRef]
8. Yang, W.S.; Park, B.W.; Jung, E.H.; Jeon, N.J.; Kim, Y.C.; Lee, D.U.; Shin, S.S.; Seo, J.; Kim, E.K.; Noh, J.H.; et al. Iodide management in formamidinium-lead-halide–based perovskite layers for efficient solar cells. *Science* **2017**, *356*, 1376–1379. [CrossRef]
9. Deng, W.; Huang, L.M.; Xu, X.Z.; Zhang, X.J.; Jin, X.C.; Lee, S.T.; Jie, J.S. Ultrahigh-Responsivity Photodetectors from Perovskite Nanowire Arrays for Sequentially Tunable Spectral Measurement. *Nano Lett.* **2017**, *17*, 2482–2489. [CrossRef]
10. Kalinin, S.V.; Spaldin, N.A. Functional Ion Defects in Transition Metal Oxides. *Science* **2013**, *341*, 858–859. [CrossRef] [PubMed]
11. Malyi, O.I.; Yeung, M.T.; Poeppelmeier, K.R.; Persson, C.; Zunger, A. Spontaneous Non-stoichiometry and Ordering in Degenerate but Gapped Transparent Conductors. *Matter* **2019**, *1*, 280–294. [CrossRef]
12. Bai, J.W.; Yang, J.; Dong, W.X.; Zhang, Y.Y.; Bai, W.; Tang, X.D. Structural and magnetic properties of perovskite $SrMnO_3$ thin films grown by molecular beam epitaxy. *Thin Solid Films* **2017**, *644*, 57–64. [CrossRef]
13. Wang, F.; Zhang, Y.Q.; Bai, Y.; Liu, W.; Zhang, H.R.; Wang, W.Y.; Li, S.K.; Ma, S.; Zhao, X.G.; Sun, J.R.; et al. Oxygen vacancy formation, crystal structures, and magnetic properties of three $SrMnO_{3-\delta}$ films. *Appl. Phys. Lett.* **2016**, *109*, 052403. [CrossRef]
14. Maurel, L.; Marcano, N.; Prokscha, T.; Langenberg, E.; Blasco, J.; Guzmán, R.; Suter, A.; Magén, C.; Morellón, L.; Ibarra, M.R.; et al. Nature of antiferromagnetic order in epitaxially strained multiferroic $SrMnO_3$ thin films. *Phys. Rev. B* **2015**, *92*, 024419. [CrossRef]
15. Patrakeev, M.V.; Bahteeva, J.A.; Mitberg, E.B.; Leonidov, I.A.; Kozhevnikov, V.L.; Poeppelmeier, K.R. Electron/hole and ion transport in $La_{1-X}Sr_xFeO_{3-\delta}$. *J. Solid State Chem.* **2003**, *172*, 219–231. [CrossRef]
16. Casais, M.T.; Alonso, J.A.; Rasines, I.; Hidalgo, M.A. Preparation, neutron structural study and characterization of $BaNbO_3$: A Pauli-like metallic perovskite. *Mater. Res. Bull.* **1995**, *30*, 201–208. [CrossRef]
17. Nadkarni, N.; Zhou, T.T.; Fraggedakis, D.; Gao, T.; Bazant, M.Z. Modeling the Metal–Insulator Phase Transition in $LixCoO_2$ for Energy and Information Storage. *Adv. Funct. Mater.* **2019**, *29*, 1902821. [CrossRef]
18. Li, T.; Deng, S.; Qi, H.; Zhu, T.; Chen, Y.; Wang, H.; Zhu, F.; Liu, H.; Wang, J.; Guo, E.J.; et al. High-Temperature Ferroic Glassy States in $SrTiO_3$-Based Thin Films. *Phys. Rev. Lett.* **2023**, *131*, 246801. [CrossRef]

19. Kan, D.; Orikasa, Y.; Nitta, K.; Tanida, H.; Kurosaki, R.; Nishimura, T.; Sasaki, T.; Guo, H.C.; Ozaki, Y.; Uchimoto, Y.; et al. Overpotential-Induced Introduction of Oxygen Vacancy in $La_{0.67}Sr_{0.33}MnO_3$ Surface and Its Impact on Oxygen Reduction Reaction Catalytic Activity in Alkaline Solution. *J. Phys. Chem. C* **2016**, *120*, 6006–6010. [CrossRef]
20. Islamov, D.R.; Zalyalov, T.M.; Orlov, O.M.; Gritsenko, V.A.; Krasnikov, G.Y. Impact of oxygen vacancy on the ferroelectric properties of lanthanum-doped hafnium oxide. *Appl. Phys. Lett.* **2020**, *117*, 162901. [CrossRef]
21. Trabelsi, H.; Bejar, M.; Dhahri, E.; Sajieddine, M.; Khirouni, K.; Prezas, P.R.; Melo, B.M.G.; Valente, M.A.; Graça, M.P.F. Effect of oxygen vacancies on $SrTiO_3$ electrical properties. *J. Alloys Compd.* **2017**, *723*, 894–903. [CrossRef]
22. Liu, Y.K.; Wong, H.F.; Lam, K.K.; Mak, C.L.; Leung, C.W. Tuning ferromagnetic properties of $LaMnO_3$ films by oxygen vacancies and strain. *J. Magn. Magn. Mater.* **2019**, *481*, 85–92. [CrossRef]
23. Lee, D.Y.; Cho, C.W.; Kim, J.W.; Bae, J.S.; Yun, H.J.; Lee, J.; Park, S.Y. Effect of oxygen vacancies in the magnetic properties of the amorphous $CoFe_2O_4$ films. *J. Non-Cryst. Solids* **2017**, *456*, 83–87. [CrossRef]
24. Chen, Y.H.; Luo, D.B.; Cao, X.Y.; Wang, Y.F.; Aung, P.; Jin, K.X.; Wang, S.H. Effect of oxygen vacancies on the electrical transport properties of conductive $Y_3Fe_5O_{12}$ films at high temperature. *J. Phys. D Appl. Phys.* **2023**, *56*, 455107. [CrossRef]
25. Zulueta, Y.A.; Dawson, J.A.; Leyet, Y.; Guerrero, F.; Anglada-Rivera, J.; Nguyen, M.T. Influence of titanium and oxygen vacancies on the transport and conducting properties of barium titanate. *Phys. Status Solidi B* **2016**, *253*, 345–350. [CrossRef]
26. Sun, H.Y.; Mao, Z.W.; Zhang, T.W.; Han, L.; Zhang, T.T.; Cai, X.B.; Guo, X.; Li, Y.F.; Zang, Y.P.; Guo, W.; et al. Chemically specific termination control of oxide interfaces via layer-by-layer mean inner potential engineering. *Nat. Commun.* **2018**, *9*, 2965. [CrossRef]
27. Becher, C.; Maurel, L.; Aschauer, U.; Lilienblum, M.; Magen, C.; Meier, D.; Langenberg, E.; Trassin, M.; Blasco, J.; Krug, I.P.; et al. Strain-induced coupling of electrical polarization and structural defects in $SrMnO_3$ films. *Nat. Nanotechnol.* **2015**, *10*, 661–665. [CrossRef]
28. Guo, H.Z.; Wang, J.O.; He, X.; Yang, Z.Z.; Zhang, Q.H.; Jin, K.J.; Ge, C.; Zhao, R.Q.; Gu, L.; Feng, Y.Q.; et al. The Origin of Oxygen Vacancies Controlling $La_{2/3}Sr_{1/3}MnO_3$ Electronic and Magnetic Properties. *Adv. Mater. Interfaces* **2016**, *3*, 1500753. [CrossRef]
29. Lei, Q.Y.; Golalikhani, M.; Davidson, B.; Liu, G.Z.; Schlom, D.G.; Qiao, Q.; Zhu, Y.M.; Chandrasena, R.U.; Yang, W.B.; Gray, A.X.; et al. Constructing oxide interfaces and heterostructures by atomic layer-by-layer laser molecular beam epitaxy. *Npj Quantum Mater.* **2017**, *2*, 10. [CrossRef]
30. Haislmaier, R.C.; Grimley, E.D.; Biegalski, M.D.; LeBeau, J.M.; Trolier-McKinstry, S.; Gopalan, V.; Engel-Herbert, R. Unleashing Strain Induced Ferroelectricity in Complex Oxide Thin Films via Precise Stoichiometry Control. *Adv. Funct. Mater.* **2016**, *26*, 7271–7279. [CrossRef]
31. Jalan, B.; Moetakef, P.; Stemmer, S. Molecular beam epitaxy of $SrTiO_3$ with a growth window. *Appl. Phys. Lett.* **2009**, *95*, 032906. [CrossRef]
32. Ohnishi, T.; Shibuya, K.; Yamamoto, T.; Lippmaa, M. Defects and transport in complex oxide thin films. *J. Appl. Phys.* **2008**, *103*, 103703. [CrossRef]
33. Bai, J.W.; Liu, Q.Q.; Wu, M.; Yang, J.; Jiang, W.; Wang, J.L.; Bai, W.; Zhang, Y.Y.; Tang, X.D.; Chu, J.H. Correlation of oxygen vacancy and Jahn–Teller polarons in epitaxial perovskite $SrMnO_3$ ultrathin films: Dielectric spectroscopy investigations. *Appl. Phys. Lett.* **2020**, *116*, 142901. [CrossRef]
34. Guzman, R.; Maurel, L.; Langenberg, E.; Lupini, A.R.; Algarabel, P.A.; Pardo, J.A.; Magen, C. Polar-Graded Multiferroic $SrMnO_3$ Thin Films. *Nano Lett.* **2016**, *16*, 2221–2227. [CrossRef]
35. Brooks, C.M.; Kourkoutis, L.F.; Heeg, T.; Schubert, J.; Muller, D.A.; Schlom, D.G. Growth of homoepitaxial $SrTiO_3$ thin films by molecularbeam epitaxy. *Appl. Phys. Lett.* **2009**, *94*, 162905. [CrossRef]
36. Tokuda, Y.; Kobayashi, S.; Ohnishi, T.; Mizoguchi, T.; Shibata, N.; Ikuhara, Y.; Yamamoto, T. Strontium vacancy clustering in Ti-excess $SrTiO_3$ thin film. *Appl. Phys. Lett.* **2011**, *99*, 033110. [CrossRef]
37. Chan, N.H.; Sharma, R.K.; Smyth, D.M. Nonstoichiometry in Undoped $BaTiO_3$. *J. Am. Ceram. Soc.* **1981**, *64*, 556–562. [CrossRef]
38. Liu, Q.Q.; Zhong, Q.L.; Bai, J.W.; Yang, J.; Huang, R.; Bai, W.; Zhang, Y.Y.; Duan, C.G.; Tang, X.D. Specific cation stoichiometry control of $SrMnO_{3-\delta}$ thin films via RHEED oscillations. *Appl. Phys. Lett.* **2021**, *118*, 232903. [CrossRef]
39. Yang, J.; Bai, W.; Zhang, Y.; Duan, C.G.; Chu, J.; Tang, X. Dielectric phenomena of multiferroic oxides at acoustic- and radio-frequency. *J. Phys. Condens. Matter* **2023**, *35*, 463001. [CrossRef]
40. Maglione, M. Free charge localization and effective dielectric permittivity in oxides. *J. Adv. Dielectr.* **2016**, *06*, 1630006. [CrossRef]
41. Lunkenheimer, P.; Loidl, A. Dielectric spectroscopy on organic charge-transfer salts. *J. Phys. Condens. Matter* **2015**, *27*, 373001. [CrossRef]
42. Lunkenheimer, P.; Krohns, S.; Riegg, S.; Ebbinghaus, S.G.; Reller, A.; Loidl, A. Colossal dielectric constants in transition-metal oxides. *Eur. Phys. J. Spec. Top.* **2010**, *180*, 61–89. [CrossRef]
43. Ahad, A.; Shukla, D.K.; Rahman, F.; Gautam, K.; Dey, K.; Majid, S.S.; Sharma, S.K.; Coaquira, J.A.H. Griffiths-like phase and charge-spin glass state in $La_{1.5}Sr_{0.5}CoO_4$. *Appl. Phys. Lett.* **2018**, *113*, 102405. [CrossRef]
44. Kagawa, F.; Mochizuki, M.; Onose, Y.; Murakawa, H.; Kaneko, Y.; Furukawa, N.; Tokura, Y. Dynamics of multiferroic domain wall in spin-cycloidal ferroelectric $DyMnO_3$. *Phys. Rev. Lett.* **2009**, *102*, 057604. [CrossRef]
45. Xu, G.; Zhong, Z.; Bing, Y.; Ye, Z.G.; Shirane, G. Electric-field-induced redistribution of polar nano-regions in a relaxor ferroelectric. *Nat. Mater.* **2006**, *5*, 134–140. [CrossRef]

46. Guerra, J.D.L.S.; Lente, M.H.; Eiras, J.A. Microwave dielectric dispersion process in perovskite ferroelectric systems. *Appl. Phys. Lett.* **2006**, *88*, 102905. [CrossRef]
47. Park, T.; Nussinov, Z.; Hazzard, K.R.; Sidorov, V.A.; Balatsky, A.V.; Sarrao, J.L.; Cheong, S.W.; Hundley, M.F.; Lee, J.S.; Jia, Q.X.; et al. Novel dielectric anomaly in the hole-doped $La_2Cu_{1-x}Li_xO_4$ and $La_{2-x}Sr_xNiO_4$ insulators: Signature of an electronic glassy state. *Phys. Rev. Lett.* **2005**, *94*, 017002. [CrossRef]
48. Chen, A.; Zhi, Y. Oxygen-vacancy-related low-frequency dielectric relaxation and electrical conduction in Bi:$SrTiO_3$. *Phys. Rev. B* **2000**, *62*, 228–236. [CrossRef]
49. Jonscher, A.K. Dielectric relaxation in solids. *J. Phys. D Appl. Phys.* **1999**, *32*, 57–70. [CrossRef]
50. Raistrick, I.D.; Franceschetti, D.R.; Macdonald, J.R. *Impedance Spectroscopy: Theory, Experiment, and Applications*; John Wiley & Sons: Hoboken, NJ, USA, 2005.
51. Savinov, M.; Bovtun, V.; Tereshina-Chitrova, E.; Stupakov, A.; Dejneka, A.; Tyunina, M. Dielectric relaxation in epitaxial films of paraelectric-magnetic SrTiO3-SrMnO3 solid solution. *Appl. Phys. Lett.* **2018**, *112*, 052901. [CrossRef]
52. Bujakiewicz-Koronskaa, R.; Nalecza, D.M.; Majcherb, A.M.; Juszynska-Galazkac, E.G.M.; Vasylechkod, L.; Markiewicze, E.; Majdaf, D.; Kalvaneg, A.; Koronskih, K. Structural, magnetic, dielectric and mechanical properties of (Ba,Sr)MnO_3 ceramics. *J. Eur. Ceram. Soc.* **2017**, *37*, 1477–1486. [CrossRef]
53. May, S.J.; Santos, T.S.; Bhattacharya, A. Onset of metallic behavior in strained $(LaNiO_3)_n/(SrMnO_3)_2$ superlattices. *Phys. Rev. B* **2009**, *79*, 115127. [CrossRef]
54. Imada, M.; Fujimori, A.; Tokura, Y. Metal-insulator transitions. *Rev. Mod. Phys.* **1998**, *70*, 1039–1263. [CrossRef]
55. Edwardst, S.F.; Anderson, P.W. Theory of spin glasses. *J. Phys. F Met. Phys.* **1975**, *5*, 965–974. [CrossRef]